Special Issue: AFOSR

JOURNAL OF COMPOSITE MATERIALS

Journal of Composite Materials
2022, Vol. 0(0) 1–11

DOI: 10.1177/00219983221140562
journals.sagepub.com/home/jcm
SAGE

"Multifunctional composites for autonomic, adaptive and self-sustaining systems". Engineering nonreciprocal wave dispersion in a nonlocal micropolar metabeam

Qian Wu[1], P Shivashankar[1], Xianchen Xu[1], Yangyang Chen[2] and Guoliang Huang[1]

Abstract

Active metamaterials with electronic control schemes can exhibit nonreciprocal and/or complex elastic coefficients that result in non-Hermitian wave phenomena. Here, we investigate theoretically and experimentally a non-Hermitian micropolar metabeam with piezoelectric elements and electronic nonlocal feed-forward control. Since the nonlocal feed-forward control breaks spatial reciprocity, the proposed metabeam supports nonreciprocal flexural wave propagation, featuring unidirectional amplification/attenuation and non-Hermitian skin effect. Theoretical homogenization modeling is developed to consider the nonlocal effect into an effective complex bending stiffness. The unidirectional wave amplification/attenuation is attributed to the energy conversion between electrical power and mechanical work. The non-Hermitian skin effect, characterized by a winding number, is the manifestation of the flexural nonreciprocity and admits an extensive number of localized bulk eigenmodes on open boundaries. The nonlocal metabeam is also employed to engineer the anomalous wave dispersion such as tunable roton-like dispersion and band tilting. The nonlocal micropolar metabeam could pave the ways for designing non-Hermitian topological mechanical metamaterials featuring programmable nonreciprocal wave transmission and engineering roton-like wave dispersion relations under ambient environments.

Keywords

nonlocal feed-forward control, non-hermitian mechanical metamaterials, nonrecirocity, non-hermitian skin effect

Introduction

Metamaterial refers to a type of artificial periodic structures, which comprises subwavelength building blocks.[1] In the past decade, mechanical metamaterials have been investigated to support emergent wave physics and applications that are not accessible in nature, such as negative refraction,[2] nonreciprocal wave propagation,[3–6] cloaking[7] and so forth. One of the most primary goals of metamaterial design is to create wave-bearing and/or topological devices to manipulate elastic and acoustic waves such as topological wave propagation and mechanical interfacial waveguiding by using engineered microstructures.[8–12] However, passive metamaterials or metastructures cannot fulfill many novel functions as practical devices because of their lack of tunability or adaptive properties. To overcome this limitation, active and/or programmable mechanical metamaterials composed of energy-generating microstructures with feedback control become a promising platform to create adaptive functional and topological materials.[13–15] On the other hand, the active metamaterials are also non-Hermitian systems which contain non-conservative forces that require an internal or external source of energy to be present.

Recently, many efforts on active metamaterials have been devoted towards the exploration of unconventional static and dynamic behavior due to non-Hermiticity, most of which focus on parity-time-reversal (PT) phase transitions and exceptional points.[14,16,17] The active spring with feedback control has been pursued to establish nonreciprocal interactions in a mechanical lattice that emulates the non-Hermitian SuSchriefferHeeger (SSH) model.[18] To physically realize those active springs, a 1D robotic

[1]Department of Mechanical and Aerospace Engineering, University of Missouri, Columbia, MO, USA
[2]Department of Mechanical and Aerospace Engineering, Hong Kong University of Science and Technology, Kowloon, Hong Kong

Corresponding author:
Guoliang Huang, Department of Mechanical and Aerospace Engineering, University of Missouri, E2410, Columbia, MO 65211, USA.
Email: huangg@missouri.edu

metamaterial including a combination of local sensing, computation, communication, and actuation was suggested to break reciprocity at the level of the local interactions between the building blocks themselves.[19] Zero-frequency edge states in the non-Hermitian topological phase and unidirectional wave amplification were demonstrated. In contrast to the ordinary topological band theory, non-Hermitian mechanical systems exhibit unique features such as band structure sensitive to boundary conditions. By introducing active springs coupled with other local deformations, non-Hermiticity of the active interaction enters the linear elasticity of a continuum solid through odd elastic moduli, which are active moduli that violate Maxwell-Betti reciprocity.[20] The odd elastic moduli when combined with anisotropy can give rise to the non-Hermitian skin effect.[21] Nonetheless, the aforementioned active systems exhibit either of the following fundamental limitations: the active nonreciprocal effects either vanish from the linear response in the quasistatic limit or they require the presence of background sources of linear or angular momentum.[15,19,22,23] The nonlinearity is another attempt in achieving wave nonreciprocity through the generation of higher-order harmonics.[24] However, it is worth stressing that nonlinearity-based nonreciprocal systems also hold a few fundamental limitations: First, a passive nonreciprocal device can support drastically different transmissions for oppositely propagating waves, but it cannot ensure isolation when the system is excited simultaneously from both sides. In addition, there is a trade-off between the degree of nonreciprocity achievable in passive, nonlinear resonators, and the wave magnitude of forward transmission.[4] To remove these obstacles, a freestanding active metabeam with piezoelectric elements and electronic feed-forward control was recently developed that gives rise to an odd micropolar elasticity. In addition, inspired by those active metamaterials with local feedback interaction, 1D and 2D elastic lattices with nonlocal feedback interactions were explored to demonstrate a series of unconventional phenomena stemming from their non-Hermiticity.[22] However, little to no work has been successful in physically realizing active metamaterials with nonlocal feedback or feed-forward control in a continuum level.

Here, we report the design, construction, and experimental demonstration of a freestanding active metamaterial with nonlocal feed-forward control. The metamaterial is constructed with piezoelectric elements mounted on a beam and controlled by nonlocal electrical circuits. The nonlocal interaction is considered into an effective complex bending stiffness which is related to the wave propagation direction, transfer function and nonlocal order. The proposed nonlocal micropolar metabeam supports nonreciprocal flexural wave amplification and attenuation and bulk localized edge modes due to their non-Hermiticity. We also experimentally show the resulting unidirectional amplification/attenuation of waves propagating through the metambeam. To gain intuition into the mechanisms of the metabeam, analytical modeling including continuum and discrete representations are used. The nonlocal metabeam is also employed to engineer the anomalous wave dispersion such as tunable roton-like dispersion. Its reciprocity can be easily maintained or broken through electrically programmable transfer functions. The tunable nonlocal micropolar metabeam with programmable feed-forward control could provide a platform for the investigation of topological phases of non-Hermitian systems.

Design of the nonlocal micropolar metabeam

We start with the design of the nonlocal micropolar metabeam. The proposed structure consists of an aluminum host beam and an array of piezoelectric patches (PZT-5A) on top and bottom of the host beam [see Figures 1(a) and (b)]. The host beam is 5 mm wide and 3 mm thick. It is made of aluminum (ρb = 2700 kg/m3, Gb = 26 GPa, Eb = 69 GPa). All the piezoelectric patches mounted on the beam are PZT-5A (ρp = 7600 kg/m^3, $\varepsilon_{33}^T = 1900\varepsilon_0$, $d_{31} = -1.75 \times 10-^{10}$C/$N$, $d_{33} = 4 \times 10-^{10}$C/$N$, $d_{15} = 5.9 \times 10-^{10}$C/$N$) with a thickness of 0.64 mm, a side length of 6.4 mm and a width of 4.9 mm. The motion of the host beam can be characterized by two independent degrees of freedom: the flexural displacement w (x) of the midplane and the rotation angle ϕ (x) of the cross section with respect to the vertical axis [see Figure 1(c)]. Each PZT patch pair performs as a sensor-actuator feed-forward loop. The actuating patches apply elongation or contraction to the top surface of the host beam, depending on the applied voltage. Conversely, the sensing patches extract voltages from the elongation and contraction of the bottom surface. The nonlocal interaction is realized by connecting the (n + a) th sensor to the nth actuator through an electronic microcontroller with a transfer function H, where a is the nonlocal order and satisfies a ≥1 for non-vanishing nonlocality [see Figure 1(c)]. As a result, the n th actuator exerts an external bending moment which is proportional to the bending deformation $\partial_x\phi(x + \delta x)$ at the $(n + a)$ th unit cell. We will demonstrate that the frequency bands of the metabeam are complex with non-Hermiticity leading to the presence of energetic gain and loss in opposite propagation directions. Such behavior is also tunable due to the programmability of H, which can be exploited to establish multiple frequency bands with interchanging nonreciprocal behavior.

Nonlocal micropolar elasticity

The equations of motion for a freestanding nonlocal micropolar beam, shown in Figure 1, are expressed as:

$$\rho\ddot{w} = \partial_x\sigma_{zx}, \tag{1}$$

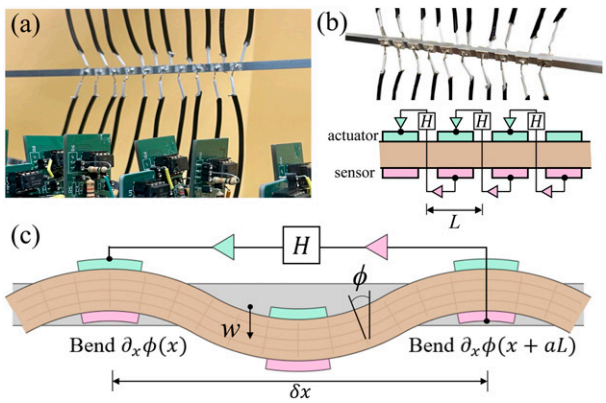

Figure 1. Design and mechanics of a nonlocal micropolar metabeam. (a) A photograph of the proposed nonlocal micropolar metabeam with a programmable electronic microcontroller system in the foreground. (b) An illustration of the full nonlocal metabeam is shown in the top panel. The bottom panel shows the schematic of a segment of the metabeam. The sensors and actuators are connected nonlocally by the transfer function H. The illustrated example here corresponds to a nearest-neighbor nonlocal configuration (a = 1). The lattice constant is L = 10 mm. (c) Schematic illustration of the mechanics of the nonlocal micropolar metabeam. The (n + a)th sensor is connected to the nth actuator through H in a periodic way.

$$I\ddot{\phi} = \partial_x M + Q, \tag{2}$$

where ρ and I are the mass density and cross-sectional moment of inertia, respectively, and Q and M are the shear force and bending moment, respectively. In particular, Q and M at x are obtained through the general constitutive relations reading,where μ and B are the shear and bending moduli of the piezoelectric metabeam without active control. C_b and C_s are the off-diagonal micropolar moduli, the feedback "(p)" represents the moduli induced by $H(\omega)$, and the shear deformation $s(x)$ and the bending curvature $b(x)$ read, respectively

$$s(x) = \partial_x w(x) - \phi(x) \tag{4}$$

$$b(x) = \partial_x \phi(x). \tag{5}$$

The local stress state possesses two components: the local contribution from the host beam with piezoelectric patches and the nonlocal contribution produced by $H(\omega)$. For a passive beam system ($H(\omega) = 0$), the off-diagonal coupling elastic moduli are zero by taking the cross-sectional local axes collinear with the principal axes of inertia and centered at the center of mass. However, this condition may not hold for active beams where the energy conservation is broken. Coupling between shear and bending can be activated through applied active forces or deformation.[25] Therefore, for general beam media including active and passive elements, we should assume the linear constitutive relation includes nonzero off-diagonal coupling elastic moduli $C_b(\omega)$ and $C_s(\omega)$. Due to the arrangement of sensor-actuator pairs in this work, the nonlocal shear barely contributes to the local shear and bending, nor does the nonlocal bending to the local one, implying $\mu^{(P)} = C_s^{(P)} = C_b^{(P)} \approx 0$. Under harmonic assumption (ω, k), equation (3) becomes

$$\begin{bmatrix} Q(\omega) \\ M(\omega) \end{bmatrix} = \begin{bmatrix} \mu(\omega) & C_b(\omega) \\ C_s(\omega) & B_{\text{eff}}(\omega) \end{bmatrix} \begin{bmatrix} s(\omega) \\ b(\omega) \end{bmatrix} = \mathbf{C}(\omega) \begin{bmatrix} s(\omega) \\ b(\omega) \end{bmatrix}, \tag{6}$$

where C_b, $C_s \approx 0$ at low frequencies, $B_{\text{eff}} = B + Pe^{ik\delta x}$ is the effective bending modulus, and p represents the nonlocal bending contribution $B^{(p)}$. For simplicity, we use a homogeneous beam model to approximate the actual piezoelectric-based metabeam considering the small geometry of the piezoelectric patches under the relative low-frequency. Typically, the constitutive tensors $\mathbf{C}(\omega)$ of the metabeam can be determined by using micromechanical approaches, which are dependent on the operating frequency in general, [25] as will be discussed later.

$$\begin{bmatrix} Q(x) \\ M(x) \end{bmatrix} = \underbrace{\begin{bmatrix} \mu(\omega) C_b(\omega) C_s(\omega) B(\omega) \end{bmatrix}}_{\text{local}} \begin{bmatrix} s(x) b(x) \end{bmatrix} + \underbrace{\begin{bmatrix} \mu^{(P)}(\omega) C_b^{(P)}(\omega) C_s^{(P)}(\omega) B^{(P)}(\omega) \end{bmatrix}}_{\text{nonlocal}} \begin{bmatrix} s(x+\delta x) b(x+\delta x) \end{bmatrix} \tag{3}$$

Nonlocal micropolar elastodynamics

Considering $\mathbf{C}$ is frequency independent at the quasistatic limit, we revisit the linearized continuum equations given in equations (1) and (2), where under the harmonic assumption of $e^{i(kx-\omega t)}$ and an instant control ($\delta t = 0$), the strain-stress relations read.

$$\begin{bmatrix} Q \\ M \end{bmatrix} = \begin{bmatrix} \mu & 0 \\ 0 & B + P(\cos k\delta x + i \sin k\delta x) \end{bmatrix} \begin{bmatrix} s \\ b \end{bmatrix}. \tag{7}$$

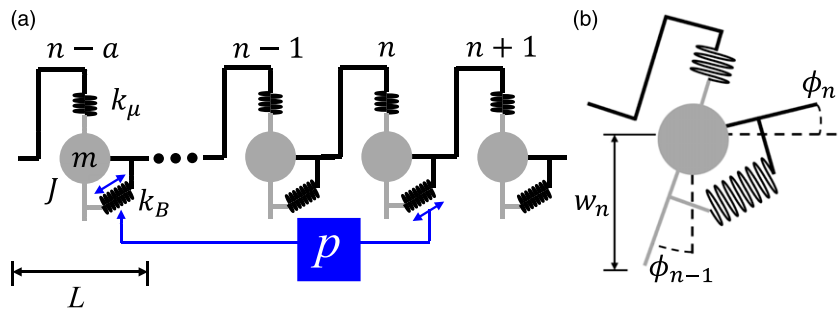

Figure 2. Discrete spring-mass representation of the nonlocal micropolar metabeam. (a) The discrete model consists of a central mass m with moment of inertial J, a Hookean spring k_μ, and a torsional spring k_B. The feedback from n th to the $(n-a)$ th unit cells is represented by p. (b) Schematic of the deformation of the n th lattice unit cell with w_n and ϕ_n denoting as its flexural displacement and rotation angle, respectively.

Combining equations (1), (2), and (7) we obtain the dispersion relation of the nonlocal metabeam as,

$$\omega^4 - \left[\frac{\mu}{I} + k^2\left(\frac{\mu}{\rho} + \frac{B_{\text{eff}}}{I}\right)\right]\omega^2 + \frac{B_{\text{eff}}\mu}{I\rho}k^4 = 0. \tag{8}$$

The above dispersion equation is complex-valued for the presence of the complex-valued nonlocal bending modulus. At a specific wave number k, we can solve for the complex ω. For the nonlocal metabeam, we conduct numerical simulations for a unit cell using COMSOL to determine all the moduli of **C** which are found approximately frequency independent at small $|k|$. Note that all the simulations included in this work involve full beam systems with PZT patches and nonlocal feed-forward control. We also use multiple mesh elements along the beam thickness, with quadratic serendipity discretization, to effectively avoid the possible shear locking issues in numerical simulations. By selecting properly prescribed strain boundaries and measuring the reaction forces, we empirically find the system parameters $B_{eff} = 8.24 \times 10^4$ kgm2/s2 and $\mu = 5.612 \times 10^9$ kg/s2. The feedback coefficient $p(\omega)$ is approximated to be $p(\omega) = \Gamma H(\omega)$ with $\Gamma = 7.5 \times 10^2$ kgm2/s2. The normalized effective mass density and moment of inertia are computed to be $\rho = 4.776 \times 10^3$ kg/m3 and $I = 3.2 \times 10^{-3}$ kgm.

A discrete representation of the nonlocal micropolar metabeam

It is also intuitive to discretize the continuous nonlocal micropolar metabeam into a discrete model.[25] Here, we consider a 1D lattice whose unit cell consists of a rigid mass, a Hookean spring and a torsional spring; see Figures 2(a) and (b). The vertical position and orientation of the n th rigid mass are represented by w_n and ϕ_n, respectively; also see Figure 2(b). The Hookean spring connected to the nth mass causes a tension force,

$$T_n = k_\mu(w_{n-1} - w_n + L\phi_{n-1}) \tag{9}$$

With $k_\mu = \mu/L$, while the torsional spring exerts a bending moment,

$$\tau_n = k_B(\phi_{n-1} - \phi_n) \tag{10}$$

With $k_B = B/L$. Since the metabeam is modulated by a nonlocal feed-forward control loop, an additional bending moment τ_n^{act} is added on the $(n-a)$ th unit cell, meaning that

$$\tau_n^{act} = p(\phi_{n-1} - \phi_n), \tag{11}$$

where $p = Pe^{ikaL}/L$. In this design, the considered uniform distribution of bending moment does not necessarily cause shear force. Therefore, considering the equilibrium conditions within each unit cell, we obtain:

$$m\ddot{\omega}_n = T_n - T_{n-1}, \tag{12}$$

$$J\ddot{\phi}_n = \tau_n - \tau_{n+1} + \tau_n^{act} - \tau_{n+1}^{act} - LT_{n+1}, \tag{13}$$

where $m = \rho L$ and $J = IL$. Combining all expressions above leads to,

$$m\ddot{\omega}_n = k_\mu(w_{n-1} - 2w_n + w_{n+1}) + Lk_\mu(\phi_{n-1} - \phi_n), \tag{14}$$

$$\begin{aligned} J\ddot{\phi}_n = {} & (k_B + p)(\phi_{n-1} - 2\phi_n + \phi_{n+1}), \\ & + Lk_\mu(w_{n+1} - w_n) - L^2k_\mu\phi_n, \end{aligned} \tag{15}$$

Note that the discrete model of the metabeam is nothing but a finite-difference version of equations (1) and (2) and should work well within the quasistatic region.

Nonreciprocity and energy cycles

We first examine the complex dispersion engineering of the nonlocal metabeam. Equation (8) admits four solutions with two of them being the evanescent modes and the other two the propagating ones. We plot analytically the lowest

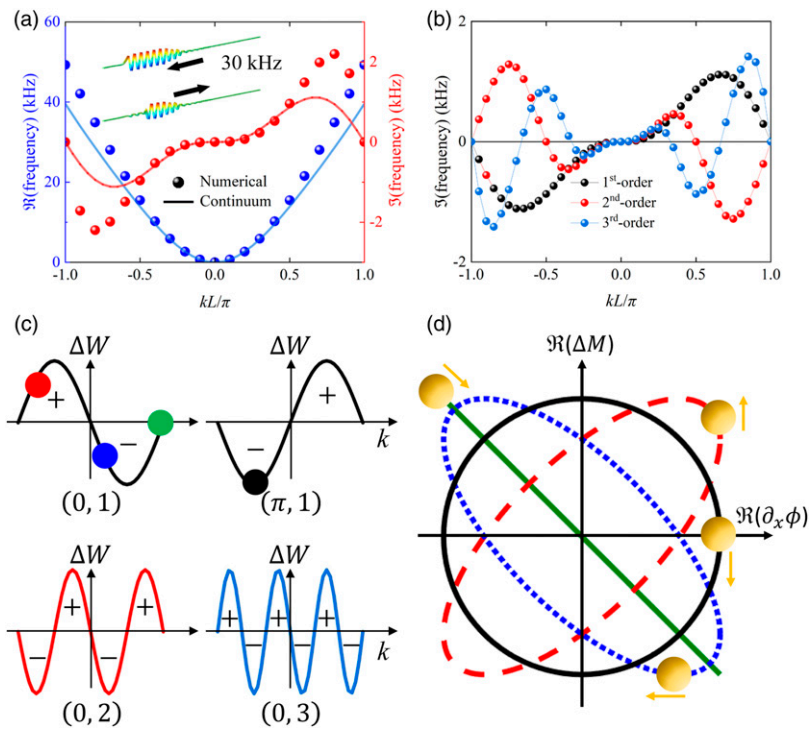

Figure 3. Complex dispersion engineering for nonreciprocal amplification and attenuation. (a) Complex dispersion for 1st-order nonlocal configuration. The solid curves are analytical results from the continuum theory. The symbols represent the numerical results from a fully coupled Finite-element software (COMSOL Multiphysics). The inset shows two representative scenarios featuring the nonreciprocity for the opposite propagation directions at 30 kHz. (b) Imaginary dispersion band for the 1st-, 2nd-, and 3rd-order nonlocalities. (c) Work done by nonlocal bending, ΔW, with $|P|e^{i\Phi_P}$ and $\delta x = aL$. Four situations are shown with different (Φ_P, a). The signs "+" and " − " correspond to the positive and negative ΔW. In particular, four representative states are selected. (d) Trajectories of the selected four states in the $\Re(\Delta W)$ - $\Re(\partial_x \Phi)$ space with $|b| = |p| = 1$. The particle direction indicates the evolution from one end of IRZ to the other.

complex band structure in the irreducible zone (IRZ) for $a = 1$ (1st-order nonlocality) and $p = 1.384 \times 10^4$ kgm2/s2 ($H = 20$) in Figure 3(a) (see the solid curves). The real part of the band structure $\Re(\omega)$ is symmetric with respect to $k = 0$, while its imaginary component $\Im(\omega)$ is antisymmetric, meaning that the amplification and attenuation of the flexural wave propagation are nonreciprocal in the x direction: flexural waves propagating in $-x$ and $+x$ undergo amplification and attenuation, respectively. Numerical eigenfrequency analysis confirms this theoretical prediction, in spite of some discrepancies at higher frequencies due to the fact that equation (8) works properly only for small $|k|$. In addition, the dispersion given by the discrete model (equations (14) and (15)) is also in good agreement with both numerical and analytical results at small $|k|$. The nonlocal order plays an important role in controlling the number of nonreciprocal amplification/attenuation regimes. As shown in Figure 3(b), 2nd- and 3rd-order nonlocalities, corresponding to the $a = 2$ and $a = 3$ scenarios, generate two and three nonreciprocal amplification/attenuation regimes along a certain propagation direction, respectively. The difference from the first-order nonlocality $a = 1$ is that waves now can be either amplified or attenuated in one direction, depending on the operating frequency (or wave number). The $a = 2$ and $a = 3$ configurations provide frequency-dependent wave transmission patterns along one propagation direction. For instance, one can realize wave attenuation at lower frequencies and wave amplification at higher frequencies along the positive wave number direction with $a = 2$, which could be potentially utilized as one additional degree of freedom for one-way flexural wave control in practical applications.

For better understanding the wave nonreciprocity, energy cycles are also studied for the metabeam. Here, we assume $P = |P|e^{i\Phi_P}$. Then, the local strain and nonlocal bending can be qualitatively expressed, respectively, as:

$$\partial_x \phi \propto e^{-i\omega t}, \tag{16}$$

$$\Delta M \propto |P|e^{i\Phi_P} e^{ik\delta x} e^{-i\omega t}, \tag{17}$$

Then, we obtain the work done by the nonlocal bending.

$$\Delta W = \Re\left\{\int_0^T i\omega\begin{pmatrix} s \\ b \end{pmatrix}^{\dagger}\begin{pmatrix} 0 & 0 \\ 0 & P \end{pmatrix}\begin{pmatrix} s \\ b \end{pmatrix}\mathrm{d}t\right\} = 2\pi|b|^2|P|\sin(\Phi_P + k\delta x), \quad (18)$$

where $T = 2\pi/\omega$ denotes the period. With non-vanishing nonlocality, i.e. $\delta x = aL \neq 0$, $\Delta W > 0$ when $\Phi_P + k\delta x \in (0, \pi)$. This physically means that the nonlocal bending ΔM does positive work, corresponding to a process where electrical energy is converted into the mechanical one. During this process, the flexural propagation experiences amplification. By contrast, $\Delta W < 0$ holds when $\Phi_P + k\delta x \in (\pi, 2\pi)$, indicating that ΔM now delivers negative work and features the attenuation behavior of the flexural propagation since mechanical energy is now converted into the electrical one. In the top panel of Figure 3(c), we schematically show the k-dependent ΔM for $\Phi_P = 0$ and π for a 1st-order nonlocal beam, which corresponds to positive and negative P. When $\Phi_P = 0$, a negative k (left propagation) experiences positive work done by the nonlocal bending, indicating amplification. As for a positive k (right propagation), the flexural waves are attenuated. This gives exactly a physical interpretation of the nonreciprocity in the metabeam system. A sign flip of p will flip the direction of the nonreciprocity. Alternatively, the sign of ΔW can also be visually determined by the trajectories of the strain-stress curves within one period in a $\Re(\Delta W)$ - $\Re(\partial_x\Phi)$ plot; see Figure 3(d). Moreover, the bottom panel of Figure 3(c) illustrate the distribution of ΔW for higher-order nonlocalities with $\Phi_P = 0$ or positive P. Sgn(ΔW) can well predict the nonreciprocal attenuation/amplification bands when compared to the results shown in Figure 2(b). Note that a local control ($\delta x = aL = 0$) can also do nonzero work, namely $\Delta W \neq 0$. However, this ΔW causes neither amplification nor attenuation, but either a hardening or softening of metabeam for both directions.

Non-Hermitian skin effect

The nonreciprocal behavior can also be determined by inverse decay length κ, which can be analytically obtained by solving equation (8) for $k = q + i\kappa$ with purely real ω, where the positive q is the propagation constant. From Figure 4(a), it can be found that $p > 0$ leads to a negative κ, corresponding to the attenuation behavior, whereas $p < 0$ results in a positive κ, corresponding to the amplification behavior. For comparison, we also obtain the numerical inverse decay length by conducting frequency-domain simulations using a finite metabeam including 60 unit cells. We emphasize that the flexural nonreciprocity of the metabeam can also be related to a non-Hermitian skin effect. For a complex frequency ω, the following topological index ν, the winding number of a dispersion band, can be defined as:

$$\nu(\omega) = \frac{1}{2\pi i}\Sigma_\alpha \oint_{-\pi/L}^{\pi/L} \frac{\mathrm{d}}{\mathrm{d}k}\log[\omega_\alpha(k) - \omega]\mathrm{d}k, \quad (19)$$

In which $\omega_\alpha(k)$ denotes the frequency of the α band (in this work it is the lowest flexural band). From a geometrical standpoint, $\nu(\omega)$ counts the number of times the loops of a dispersion band over the IRZ encircles the selected frequency. Its sign is dependent of the handedness of the loops: $\nu(\omega) > 0$ if the rotation about the selected frequency is clockwise; $\nu(\omega) < 0$ otherwise. A non-zero $|\nu(\omega)|$ features the existence of localized bulk eigenmodes, while sgn ($\nu(\omega)$) determines which side the eigenmodes are localized on. In Figures 4(b) and (c), we plot the dispersion loops for $p < 0$ and $p > 0$, respectively. Comparison between the simulations and continuum theory is illustrated as well to show their good agreement for small $|k|$. In the two cases, one can find $\nu(\omega) = -1$ and $\nu(\omega) = 1$. Eigenmodes encircled by the $\nu(\omega) = -1$ loop are localized on the right boundary of the metabeam, whereas $\nu(\omega) = 1$ leads to localized eigenmodes on the left boundary; see also the confirmation given by Figure 4(d) from numerical eigenfrequency analysis.

Band tilting

The transfer function H can also involve nonzero phase difference, i.e. arg(H) $\neq 0$. When arg(H) $= \pm\pi/2$, H becomes purely imaginary. Then, from equation (7), it can be seen that the effective bending stiffness $\Re(B_{\mathrm{eff}})$ becomes direction dependent. In particular, its imaginary part vanishes only at $kL = \pi/2$. Similar to the nonlocal metabeam here, the reported odd-elasticity local platform with imaginary-valued control can also exhibit directional bending stiffness, but without amplification or attenuation across the entire IRZ, thus supporting free wave propagation. Figure 5(a) shows $\Re(\omega)$ is asymmetric when $H = 40i$ or equivalently $p = 5.1i \times 10^4$ kgm2/s2. This means that the left- and right-going waves exhibit different group velocities, showing band tilting phenomenon. It is also seen that the numerical and analytical results match well at small $|k|$. To further examine the band tilting, we conduct harmonic simulations for incidence from both directions at 9.211 kHz, and the computed phase distributions of the flexural waves (arg(w) = $1i \times \log[w/|w|]$) are illustrated in Figure 5(b). The band tilting effect is numerically observed from the wavelength difference.

Experimental demonstration

We fabricated a finite nonlocal metabeam consisting of 10 unit cells (a total length of $L_t = 100$ mm) and 9 active nonlocal feed-forward loops on a 6-foot-long aluminum host beam, as shown in Figure 6(a). The incidences from both sides are excited by two PZT-5A transducers connected to an amplifier and arbitrary

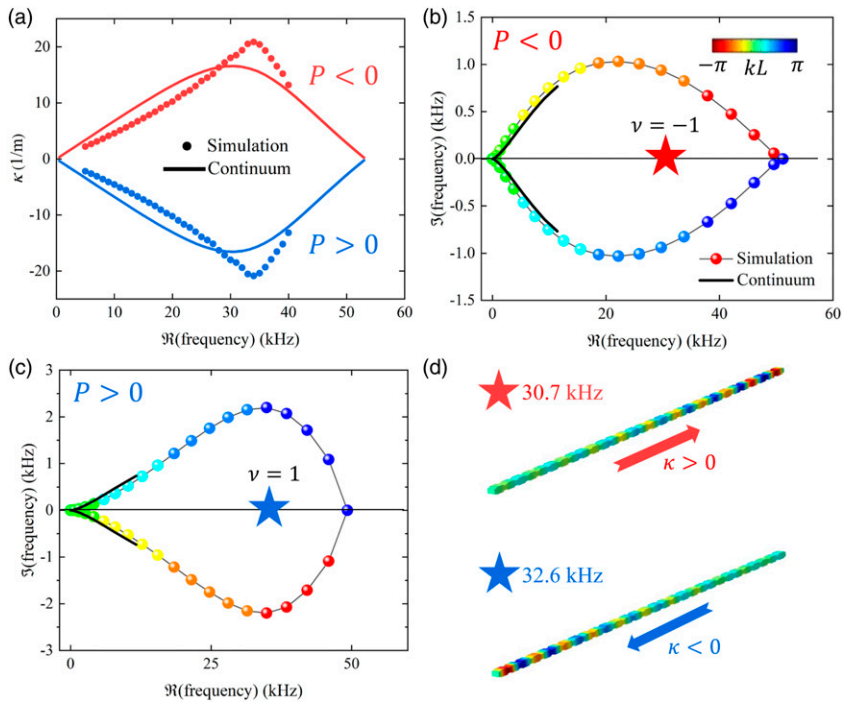

Figure 4. Non-Hermitian skin effect. (a) Calculation of the inverse decay length κ using COMSOL frequency-domain simulations (dotted) and analytical approach (solid) when $p > 0$ and $p < 0$. (b, c) The complex dispersion bands are displayed for (b) $p < 0$ and (c) $p > 0$. The winding number of each scenario ν is indicated. Comparison between the numerical simulations and continuum theory is shown. For both scenarios, two representative modes encircled by the two loops are selected. (d) The corresponding field distributions of the two selected modes feature the amplification and suppression of flexural waves.

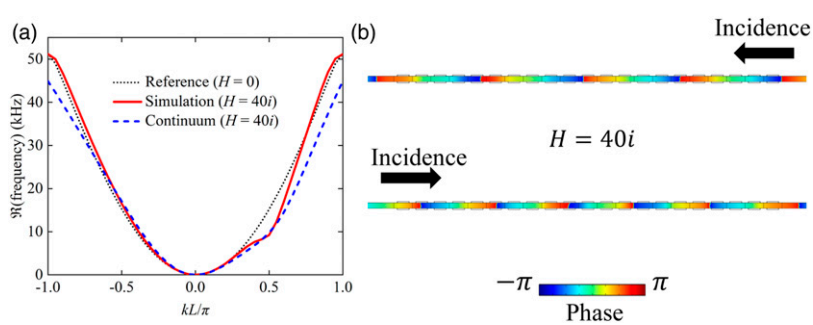

Figure 5. Band tilt induced by nonlocality. (a) The real spectrum for $H = 40i$ is shown accompanied by the comparison between the reference in absence of active loops (black dotted), eigenfrequency simulation (red solid) and the continuum theory by equation (7) (blue dashed). (b) Phase distributions of the right- and left-going flexural waves through the metabeam section at 9.211 kHz. The phase is defined as $\arg(w) = 1i \times \log[w/|w|]$. Only the phase changes within the host beam are illustrated.

function generator (AFG). The measurement and post-processing are implemented by a commercial laser vibrometer (PSV-400). The excitation is a 10-cycle tone burst signal centered at 20 kHz. The transfer function, which is realized by the circuits shown in Figure 6(b), reads

$$H(\omega) = \frac{H_0}{(i\omega/\omega_0)^2 + 2\eta(i\omega/\omega_0) + 1}, \tag{20}$$

where the cutoff frequency $\omega_0 = 2\pi \times 33.53$ kHz, the damping coefficient $\eta = 0.41$ and $H_0 = -22.5$. The experimental specifications are listed as follows: R1 = 1 MΩ, R2 = 1.5 kΩ, R3 = 6.8 kΩ, R6 = 1 kΩ, R7 = 22 kΩ, C1 = 1 nF, C2 = 4.7 nF, C3 = 0.47 nF, and Op-amp OPA445. This transfer function is plotted in Figure 6(c). Note that we use a second-order low-pass filter in the experiments since it helps stabilize the experiments by filtering out high-frequency

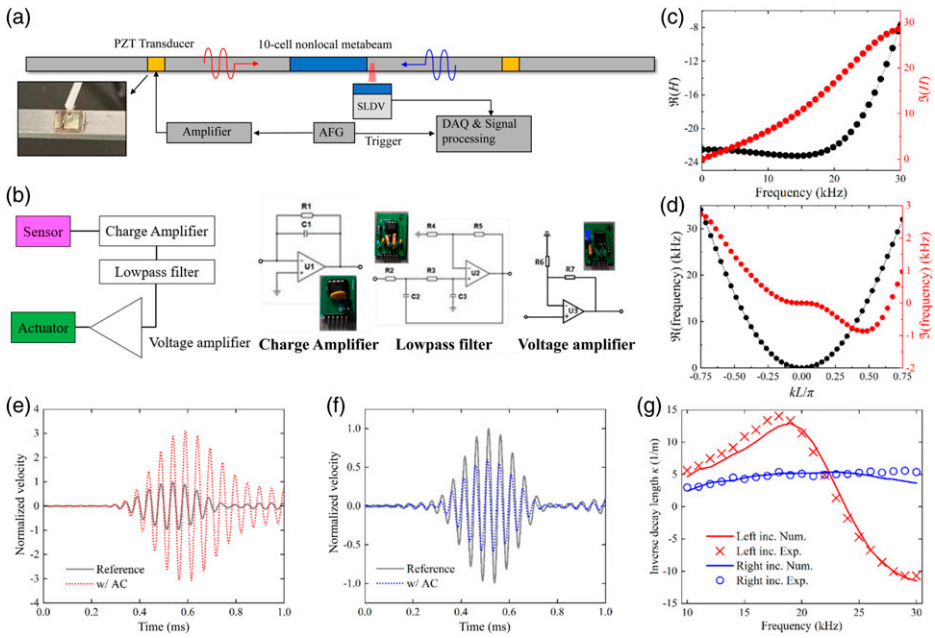

Figure 6. Experimental demonstration of nonreciprocity. (a) Schematic of the experimental setup including a 1st-order nonlocal metabeam of 10 unit cells modulated by 9 active loops. (b) The schematic of the electrical control circuit system and the circuit diagrams of individual components. (c) Complex experimental transfer function given in equation (20). (d) Complex dispersion diagram for the experimental transfer function in (c). (e, f) Measured transient velocity wave signal at the output for both incident directions. The red and blue curves represent the left and right incidences, respectively, while the gray ones are reference signals when the active control is turned off. The results with active control are normalized the maximum of the respective references. (g) Comparison of the inverse decay length κ between the experiments (symbols) and numerical transient analyses (solid) with the same transfer function as in the experiments. The left/right incidence corresponds to the right/left-going wave.

noise which is experimentally inevitable. This filter leads to the complex frequency-dependent transfer function given in equation (20). It is essential to point out that the experimental testing with such a transfer function $H(\omega)$ corresponds simply to the combination of the discussed scenarios with purely real (Figures 3(a) and 3(b)) and purely imaginary (Figure 5) transfer functions. While the frequency dependence of $H(\omega)$ simply leads to frequency-dependent nonreciprocal amplification and attenuation rates and band tilting. Specifically, the nonzero imaginary component of the transfer function, $\Im(H(\omega))$ leads to asymmetric complex dispersion (Figure 6(d)), due to the band tilting. The dispersion asymmetry further results in the difference in positive/negative damping along opposite directions. Figure 6(d) shows that the right-going flexural waves initially experience amplification due to negative imaginary frequency below about 24 kHz. Above this frequency, attenuation is expected. On the contrary, the left-going waves are attenuated across the frequency range of interest, simply due to the imaginary frequency being always positive.

For experimental validation, we use two piezoelectric (PZT-5A) actuators, each for one side, to excite flexural incidence from both sides. The probed vibration dynamics along the opposite directions at 20 kHz confirms the nonreciprocity, as shown in Figures 6(e) and (f). The magnitude of the left-incident wave at 20 kHz is amplified roughly by 232%, whereas that of the right-incident wave is suppressed by about 40%. The results suggest that despite the asymmetry in the complex dispersion, the nonreciprocal wave amplification and attenuation can still be observed for flexural waves, but at unbalanced amplification and attenuation rates in general along the opposite directions. Note that the current system cannot directly measure the rotating degrees of the structure. However, according to the micropolar (Timoshenko) beam theory, the measured bending moment can be measured and is proportional to the second derivative of the rotating angle.

To examine the inverse decay length of the metabeam, we plot the comparison between experiments and numerical simulations using $\kappa = \pm\ln(v_{norm}^{max})/L_t$ for both left- and right-incident waves in Figure 6(g), where v_{norm}^{max} is the maximum magnitude of the normalized velocity wave field. Good agreement can be found between the experiments and the numerical simulations that carry the same transfer function as the one in the experiments. A value of $\kappa > 0$ implies amplification of the right-going waves with positive k. On the contrary, A value of $\kappa > 0$ implies attenuation of the left-going waves with negative k. A closer

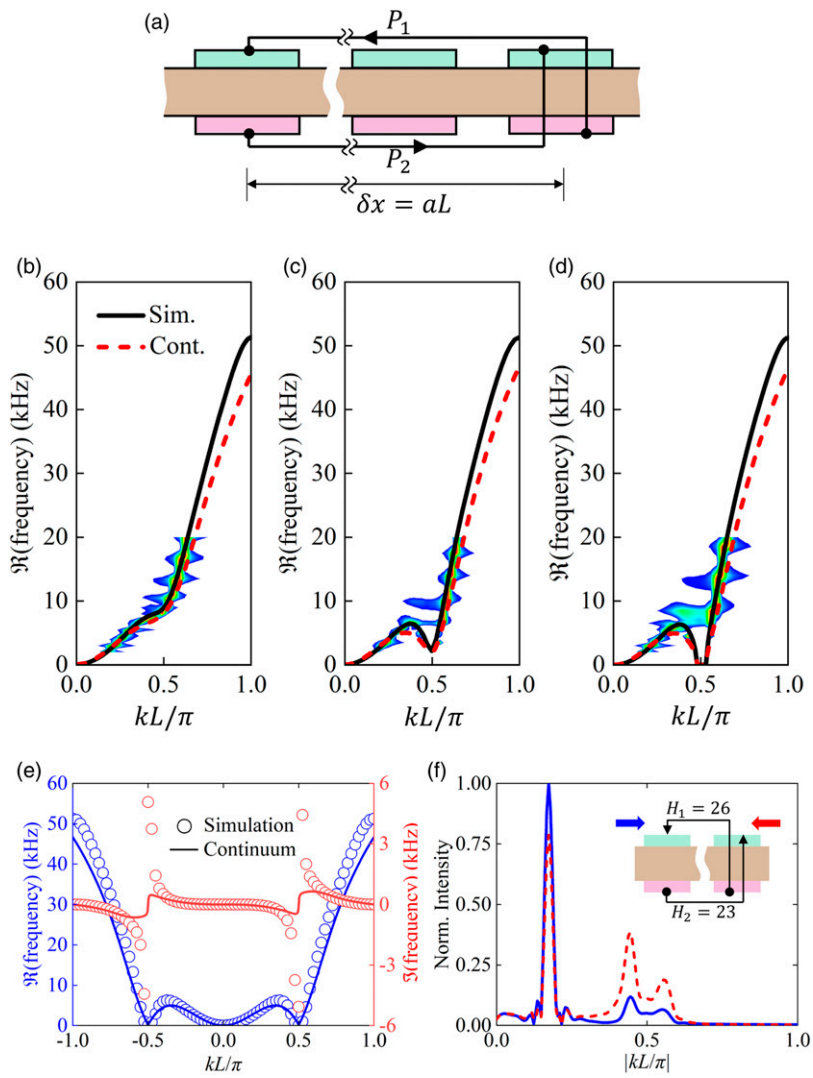

Figure 7. Reciprocal and nonreciprocal roton-like dispersion. (a) Schematic illustration of the nonlocal realization of the roton-like dispersion with a toggle between reciprocity and nonreciprocity. (b–d) Reciprocal roton-like dispersion relations enabled by $H_1 = H_2 = H$ or equivalently $P_1 = P_2 = P$. The change of the $\Re(\omega)$ band is shown when (b) $H = 20$, (c) $H = 23.5$, and (d) $H = 24$. The black and red curves represent the eigenfrequency simulation and continuum theory. The color fills are the FFT results. (e) Nonreciprocal roton-like dispersion relations enabled by $H_1 = 26$ and $H_2 = 23$. Comparison of the complex spectra between simulation and continuum theory is shown. (f) The normalized FFT-based intensity spectrum for the propagation of two opposite directions within the nonreciprocal roton-like configuration at 2 kHz.

observation of the calculated κ reveals that the nonreciprocal amplification does not always take place within the entire spectrum. Above 23.5 kHz, both left- and right-going waves undergo suppression. This has been explained previously in Figure 6(d) by the choice of the low-pass filter which causes band tilts of the complex dispersion by the nonzero $\Im(H(\omega))$. Nevertheless, the nonreciprocity of the nonlocal metabeam is evidently validated by the experiments. Similar observations are also available with higher-order nonreciprocity. Specifically, more than one nonreciprocal amplification band regions will be found.[22]

Nonreciprocal roton-like dispersion

Roton dispersion relations initially found in correlated quantum systems at low temperatures were recently developed and investigated in mechanical and acoustic systems. One of the prominent features is multiple eigenmodes supported at a single frequency, featuring net negative energy flows which are analogous to the so-called "return flow." Up to now, there have been mainly two approaches to achieving the roton-like mechanical and acoustic bands: chiral[26] and nonlocal interactions.[27,28] Here, we emphasize that with the nonlocal metabeam design, both reciprocal and

nonreciprocal roton-like dispersion relations can be observed with the help of extra nonlocal degree of freedom.

Figure 7(a) schematically illustrates the functional unit capable of achieving both reciprocal and nonreciprocal roton-like behaviors. Instead of having a single nonlocal feed-forward loop, the design now involves two loops (P_1 and P_2) with the opposite nonlocal orders, leading to:

$$B_{\text{eff}} = B + P_1 e^{ik\delta x} + P_2 e^{-ik\delta x}, \tag{21}$$

The idea of using two loops is to accommodate a toggle function between roton-like reciprocity and nonreciprocity. In Figures 7(b) to (d), the formation of the reciprocal roton-like dispersion is first demonstrated in a 2nd-order nonlocal configuration ($a = 2$), with $P_1 = P_2 = P$. Good agreement between numerical and analytical analyses validates the theoretical model in the continuum region. The roton-like dispersion appears when H exceeds about 20. Once it reaches roughly 23.8, the band touches $\omega = 0$ at a critical point at $kL = 0.5\pi$, because B_{eff} reaches zero; see equation (8). Within this range, only one roton minimum survives and three eigenmodes exist at a single frequency, with one of them exhibiting negative group velocity v_g. Continuing increasing H eventually induces a vertical bandgap within which flexural propagation at certain k is forbidden. This can also be interpreted as the emergence of negative effective bending stiffness across the certain range of k, similar to the conventional scenarios where single or double negative constitutive parameters take place in certain frequency ranges. Note that the numerically determined p is no longer in linear relation with H due to the double feed-forward controls and the value selection of H, vastly different from what we have seen in the previous sections. Overall, the roton-like behavior presented here shows similarity with those reported in three-dimensional mechanical metamaterials, since the nonlocal feedback control discussed here is equivalent to a reciprocal next-nearest-neighbor interaction. The fundamental difference lies in the realization of the nonlocal interactions: the design senses the nonlocal strain fields whereas the existing studies utilize passive reciprocal on-site interactions. Moreover, similar to those passive designs, [27] increasing the nonlocal order will also increase the number of roton minimums.

What is more compelling is that the nonlocal metabeam is also capable of realizing nonreciprocal roton-like dispersion, or in other words, a roton-like behavior with unidirectional amplification/attenuation, which has not been reported yet. To achieve it, two unbalanced transfer functions $H_1 \neq H_2$ are required. As shown in Figure 7(e), we plot the complex spectra for $H_1 = 26$ and $H_2 = 23$ using both numerical modeling and continuum theory given by equation (7). We confirm this novel behavior by examining the wave number dependent intensity difference between the two opposite directions at 2 kHz, as displayed by Figure 7(f); also see the inset of Figure 7(f), where a fast Fourier transform (FFT) is adopted on the spatial flexural displacements collected in an 81-unit-long metabeam for both directions. Specifically, the magnitude of the first positive-v_g mode is enhanced in $+x$ due to the negative $\Im(\omega)$. On the contrary, the second positive-v_g mode and the negative-v_g one featuring "return flow" are amplified in $-x$. This observation clearly verifies the validity of the nonreciprocal roton-like mechanical behavior. Note that the switch between the reciprocal and nonreciprocal configurations can be done simply by adjusting the nonlocal feed-forward control loops, possessing potential tunability.

Conclusion

We study the active metabeam enabled by nonlocal feed-forward control, providing a physical realization of the nonlocal micropolar elastic media. Both the continuum and discrete models are provided to characterize the complex band structure under the continuum limit. The nonreciprocal flexural wave amplification and attenuation are numerically demonstrated and also experimentally validated. This odd wave propagation behavior is attributed to the work done by the nonlocal bending, which is described as the exchange between mechanical energy and external electrical power. The non-Hermitian skin effect of the finite system is demonstrated and interpreted by the topology of the complex dispersion band. In addition, implementing a purely imaginary transfer function leads to the band tilting of the real spectrum. Lastly, by increasing the nonlocal degree of freedom, the roton-like mechanical dispersion with tunable options between reiciprocity and nonreciprocity is numerically verified. The nonlocal metabeam could serve as a power platform for engineering different topological wave dispersions and investigating various types of wave dynamics under the framework of non-Hermitian system.

Declaration of conflicting interests

The author(s) declared no potential conflicts of interest with respect to the research, authorship, and/or publication of this article.

Funding

The author(s) disclosed receipt of the following financial support for the research, authorship, and/or publication of this article: This work is supported by the Air Force Office of Scientific Research under Grant No. AF 9550-18-1-0342 and AF 9550-20-1-0279 with Program Manager Dr Byung-Lip (Les) Lee.

ORCID iD

Guoliang Huang https://orcid.org/0000-0002-6238-6127

References

1. Smith DR, Pendry JB and Wiltshire MC. Metamaterials and negative refractive index. *Science* 2004; 305(5685): 788–792.
2. Zhu R, Liu X, Hu G, et al. Negative refraction of elastic waves at the deep-subwavelength scale in a single-phase metamaterial. *Nat Communications* 2014; 5(1): 1–8.
3. Marconi J, Riva E, Di Ronco M, et al. Experimental observation of nonreciprocal band gaps in a space-time-modulated beam using a shunted piezoelectric array. *Phys Rev Appl* 2020; 13(3): 031001.
4. Nassar H, Yousefzadeh B, Fleury R, et al. Nonreciprocity in acoustic and elastic materials. *Nat Rev Mater* 2020; 5(9): 667–685.
5. Wu Q, Chen H, Nassar H, et al. Non-reciprocal rayleigh wave propagation in space-time modulated surface. *J Mech Phys Sol* 2021; 146: 104196.
6. Xu X, Wu Q, Chen H, et al. Physical observation of a robust acoustic pumping in waveguides with dynamic boundary. *Phys Review Letters* 2020; 125(25): 253901.
7. Nassar H, Chen Y and Huang G. A degenerate polar lattice for cloaking in full two-dimensional elastodynamics and statics. *Proc R Soc A* 2018; 474(2219): 20180523.
8. Chen H, Nassar H and Huang G. A study of topological effects in 1d and 2d mechanical lattices. *J Mech Phys Sol* 2018; 117: 22–36.
9. Huber SD, Topological mechanics. *Nat Phys* 2016; 12(7): 621–623.
10. Mousavi SH, Khanikaev AB and Wang Z. Topologically protected elastic waves in phononic metamaterials. *Nat Communications* 2015; 6(1): 1–7.
11. Wu Q, Chen H, Li X, et al. In-plane second-order topologically protected states in elastic kagome lattices. *Phys Rev Appl* 2020; 14(1): 014084.
12. Yu SY, He C, Wang Z, et al. Elastic pseudospin transport for integratable topological phononic circuits. *Nat Communications* 2018; 9(1): 1–8.
13. Chen Y, Li X, Nassar H, et al. A programmable metasurface for real time control of broadband elastic rays. *Smart Mater Structures* 2018; 27(11): 115011.
14. Shi C, Dubois M, Chen Y, et al. Accessing the exceptional points of parity- time symmetric acoustics. *Nat Communications* 2016; 7(1): 1–5.
15. Trainiti G, Xia Y, Marconi J, et al. Time-periodic stiffness modulation in elastic metamaterials for selective wave filtering: theory and experiment. *Phys Review Letters* 2019; 122(12): 124301.
16. Hou Z and Assouar B. Tunable elastic parity-time symmetric structure based on the shunted piezoelectric materials. *J Appl Phys* 2018; 123(8): 085101.
17. Wu Q, Chen Y and Huang G. Asymmetric scattering of flexural waves in a parity-time symmetric metamaterial beam. *The J Acoust Soc America* 2019; 146(1): 850–862.
18. Ghatak A, Brandenbourger M, Van Wezel J, et al. Observation of non-hermitian topology and its bulk-edge correspondence in an active mechanical metamaterial. *Proc Natl Acad Sci* 2020; 117(47): 29561–29568.
19. Brandenbourger M, Locsin X, Lerner E, et al. Nonreciprocal robotic metamaterials. *Nat Communications* 2019; 10(1): 1–8.
20. Scheibner C, Souslov A, Banerjee D, et al. Odd elasticity. *Nat Phys* 2020; 16(4): 475–480.
21. Scheibner C, Irvine WT and Vitelli V. Non-hermitian band topology and skin modes in active elastic media. *Phys Rev Lett* 2020; 125(11): 118001.
22. Rosa MI and Ruzzene M. Dynamics and topology of non-hermitian elastic lattices with non-local feedback control interactions. *New J Phys* 2020; 22(5): 053004.
23. Sirota L, Ilan R, Shokef Y, et al. Non-newtonian topological mechanical metamaterials using feedback control. *Phys Rev Lett* 2020; 125(25): 256802.
24. Wei L, Wang Y and Wang Y. Nonreciprocal transmission of nonlinear elastic wave metamaterials by incremental harmonic balance method. *Int J Mech Sci* 2020; 173: 105433.
25. Chen Y, Li X, Scheibner C, et al. Realization of active metamaterials with odd micropolar elasticity. *Nat Communications* 2021; 12(1): 1–12.
26. Kishine J, Ovchinnikov A and Tereshchenko A. Chirality-induced phonon dispersion in a noncentrosymmetric micropolar crystal. *Phys Rev Lett* 2020; 125(24): 245302.
27. Chen Y, Kadic M and Wegener M. Roton-like acoustical dispersion relations in 3d metamaterials. *Nat Communications* 2021; 12(1): 1–8.
28. Iglesias Martinez JA, Gross MF, Chen Y, et al. Experimental observation of roton-like dispersion relations in metamaterials. *Sci Advances* 2021; 7(49): eabm2189.